Two Marine Heatwave (MHW) Variants under a Basinwide MHW Conditioning Mode in the North Pacific and Their Atlantic Associations

YU ZHAO[a] AND JIN-YI YU[a]

[a] *Department of Earth System Science, University of California, Irvine, California*

(Manuscript received 17 March 2023, in final form 14 September 2023, accepted 15 September 2023)

ABSTRACT: During 2013–16 and 2018–22, marine heatwaves (MHWs) occurred in the North Pacific, exhibiting similar extensive coverage, lengthy duration, and significant intensity but with different warming centers. The warming center of the 2013–16 event was in the Gulf of Alaska (GOA), while the 2018–22 event had warming centers in both the GOA and the coast of Japan (COJ). Our observational analysis indicates that these two events can be considered as two MHW variants induced by a basinwide MHW conditioning mode in the North Pacific. Both variants were driven thermodynamically by atmospheric wave trains propagating from the tropical Pacific to the North Pacific, within the conditioning mode. The origin and propagating path of these wave trains play a crucial role in determining the specific type of MHW variant. When a stronger wave train originates from the tropical central (western) Pacific, it leads to the GOA (COJ) variant. The cross-basin nature of the wave trains enables the two MHW variants to be accompanied by a tripolar pattern of sea surface temperature anomalies in the North Atlantic but with opposite phases. The association of these two MHW variants with the Atlantic Ocean also manifests in the decadal variations of their occurrence. Both variants tend to occur more frequently during the positive phase of the Atlantic multidecadal oscillation but less so during the negative phase. This study underscores the importance of cross-basin associations between the North Pacific and North Atlantic in shaping the dynamics of North Pacific MHWs.

KEYWORDS: Atmosphere; North Atlantic Ocean; North Pacific Ocean; Rossby waves; Heat wave; Sea surface temperature

1. Introduction

Marine heatwaves (MHWs) are anomalous warming events of sea surface water that last for an extended period (Hobday et al. 2016). A peculiar and exceptional MHW event unfolded in the North Pacific in 2013, persisting for 3 years and culminating in a peak surface warming of over 2°C (Fig. 1a), with a depth of influence reaching a staggering 180 m below the ocean surface. Dubbed the "Pacific Warm Blob" (Bond et al. 2015; Hu et al. 2017), this event had far-reaching impacts on coastal ecosystems and North American climate (Whitney 2015; Peterson et al. 2015; Robinson 2016; Gentemann et al. 2017; Frölicher and Laufkötter 2018), owing to its unprecedented strength, prolonged duration, and extensive ocean area coverage. Extensive research efforts were undertaken to comprehend the underlying causes that led to its occurrence (e.g., Bond et al. 2015; Di Lorenzo and Mantua 2016; Amaya et al. 2016; Hu et al. 2017; Liang et al. 2017; J. Shi et al. 2022; Amaya et al. 2021). Two years after the event, another long-lasting, high-intensity, and large-area MHW event emerged and lasted from 2018 to 2022 (Fig. 1b). The peak magnitude of this MHW, reaching 2.5°C as determined from monthly data (Amaya et al. 2020; Scannell et al. 2020), is comparable to that of the 2013–16 event. This event also produced significant impacts on marine ecosystems in the North Pacific, including limiting the phytoplankton growth in the northwest Pacific by high temperatures and low nutrient waters, increasing salmon mortality, and reducing fisheries off the coast of Japan (Cheung and Frölicher 2020; von Biela et al. 2022). Despite sharing similar anomaly features in sea surface temperature (SST), such as extensive basinwide coverage, a prolonged duration spanning multiple years, and a remarkable amplitude, these two MHWs had different warming centers. The 2013–16 MHW had its warming center around the Gulf of Alaska (GOA) throughout the event, while the 2018–22 MHW showcased dual warming centers, with one over the GOA (Chen et al. 2021) and the other off the coast of Japan (COJ) (Kuroda and Setou 2021). Notably, the SST warming center shifted completely to the COJ region during certain periods of the 2018–22 event, such as in 2018 and the latter half of 2021 (see Fig. 1b). Although warming over the COJ region was also observed during the early period of the 2013–16 MHW, the duration was much shorter and the intensity weaker in comparison.

The 2013–16 MHW was suggested to be primarily driven by atmospheric forcing, specifically an unusually robust high pressure system that persisted over the North American coast for an extended period (Swain et al. 2014; Hassan and Nayak 2020). In addition to atmospheric forcing, there are also studies (Amaya et al. 2021; H. Shi et al. 2022) that suggest that the shallowing of the mean mixed layer (ML) depth will lead to a stronger temperature response, making MHW more frequent and more intense. The anomalous high attenuated surface wind speeds and suppressed latent heat release from the ocean surface led to the warming of the seawater over the

Supplemental information related to this paper is available at the Journals Online website: https://doi.org/10.1175/JCLI-D-23-0156.s1.

Corresponding author: Jin-Yi Yu, jyyu@uci.edu

DOI: 10.1175/JCLI-D-23-0156.1

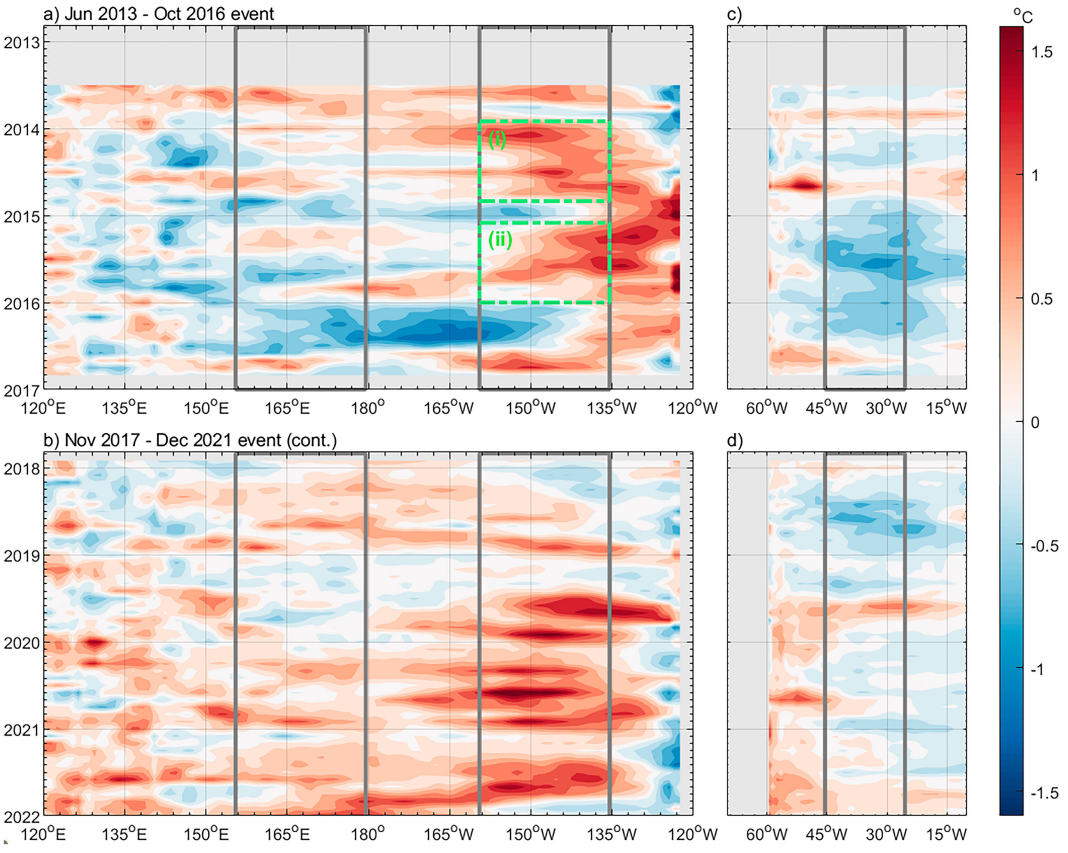

FIG. 1. Evolution of SST anomalies (SSTAs) across the (left) North Pacific (averaged between 37.5° and 47.5°N) and (right) North Atlantic (averaged between 50° and 60°N) during the (a),(c) 2013–16 MHW and (b),(d) 2018–22 MHW. The vertical gray lines in (a) and (b) mark the longitudinal ranges of the Gulf of Alaska (GOA; 160°–135°W) and coast of Japan (COJ; 155°E–180°) regions. The green dashed boxes represent the GOA (i) (from November 2013 to October 2014) and GOA (ii) (from February to December 2015) periods analyzed in Fig. 14. Vertical gray lines in (c) and (d) mark the longitudinal ranges of the Atlantic cold spell (45°–25°W).

GOA. Liang et al. (2017) further emphasized that this anomalous high is part of a large-scale circulation anomaly pattern in the atmosphere that spanned across the North Pacific, the North American continent, and the North Atlantic. They suggested that the Pacific MHW can be considered and studied as a local response to a hemisphere-scale atmospheric circulation anomaly. As pointed out by Liang et al. (2017), the circulation anomaly within the North Pacific sector is characterized by a poleward-propagating wave train that emanated from the tropical Pacific into North America. This wave train is evident in the anomaly pattern of 200-hPa geopotential height (Z200) over the 2013–16 MHW (Fig. 2a). We should note that the zonal-mean values of Z200 were removed from the anomalies to better reveal wave train patterns in Fig. 2.

An anomalous high also appeared during the 2018–22 MHW, but its center was extended from the GOA to COJ regions (Fig. 2b). This anomalous high similarly can suppress latent heat release and cause underneath surface oceans to warm (Amaya et al. 2020; Chen et al. 2021; Ge et al. 2023), particularly in the GOA and COJ regions. There are indications that the anomalous highs over the GOA or COJ region are also parts of two atmospheric wave trains. One of them seems to emanate from the tropical central Pacific toward North America and produce the anomalous high over the GOA region, similar to the one observed during the 2013–16 MHW, while the other seems to emanate from the tropical western Pacific toward the North Pacific and produce the anomalous high over the COJ region. Both the 2013–16 and 2018–22 MHWs may be considered as similar types of wave train–driven MHW in the North Pacific but with their warming centers shifted due to the different wave train paths. The generation dynamics of the North Pacific MHW may be studied from the view of extratropical ocean responses to atmospheric wave trains.

Liang et al. (2017) also suggested that the atmospheric circulation anomaly associated with the 2013–16 MHW extended into the North Atlantic to induce accompanied SST anomalies (SSTAs) in the North Atlantic through surface heat fluxes. They argued that this cross-basin nature of the anomalous atmospheric circulation is a reason why an Atlantic cold spell was observed during the 2013–15 Pacific Warm Blob (Josey et al. 2018), which can be seen in Fig. 1c. They

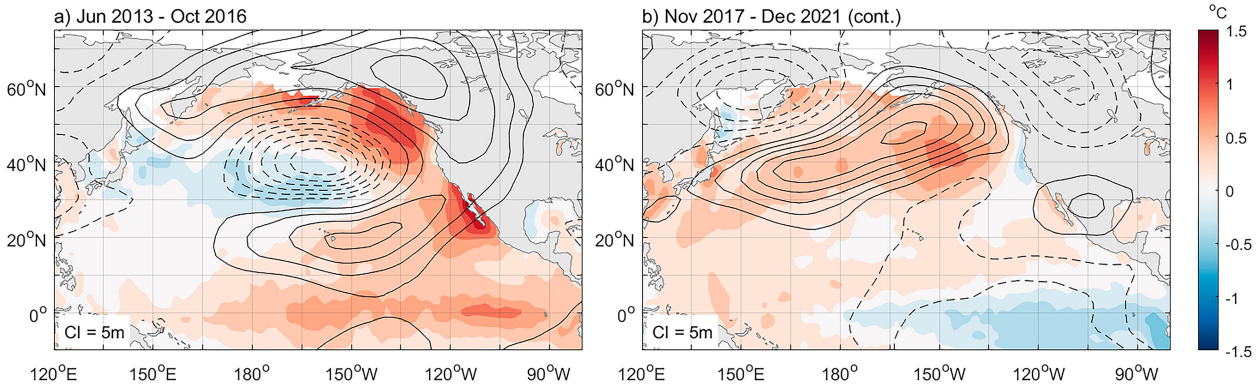

FIG. 2. Mean anomalies of SST (shading; °C) and geopotential height at 200 hPa (Z200; contours; m) averaged throughout the (a) 2013–16 and (b) 2018–22 MHW. Contour intervals are 5 m for Z200 as labeled (i.e., "CI") and solid lines represent positive values and dashed lines for the negative, with the linear trend removed. The zonal-mean values of Z200 were removed from the anomalies shown in (a) and (b) to better reveal wave train patterns in this case study.

showed that the co-occurrence of the Pacific Warm Blob and Atlantic cold spell was observed in four additional prolonged Pacific Warm Blob events (i.e., with a duration of more than 24 months), including the events of 1956–58, 1961–63, 1985–87, and 1989–95. However, we noticed that an Atlantic cold spell was observed in the 2018–22 Pacific MHW only when the warming center was located close to the GOA region, but an Atlantic warming anomaly was observed during the middle part of 2019 and the second half of 2021 when the warming center shifted more toward the COJ region. This is another interesting difference between the 2018–22 and 2013–16 MHWs.

The similarities and differences between these two recent prolonged and strong Pacific MHW events raise a possibility that there may exist two specific variants of MHWs in the North Pacific. These variants are likely influenced by atmospheric wave train propagation in an SST "conditioning" mode in the North Pacific. Furthermore, the cross-basin nature of this wave train allows the Pacific MHW event to be associated with significant North Atlantic SST warming or cooling events, depending on the variant of the MHW. In this study, we conducted observational analyses to examine these possibilities. The structure of this paper is as follows: section 2 outlines the data and methods used in the study. Section 3 presents evidence for a basinwide MHW "conditioning" mode in the North Pacific and the MHW variants it supports. Section 4 examines the driving mechanisms behind the variants and their associated North Atlantic SST conditions. Finally, section 5 summarizes and discusses the results, along with proposed further research directions.

2. Data and methods

In this study, all the analyses were performed with monthly data. Two datasets were used to provide the monthly ocean information, and another two datasets were used to provide the monthly atmospheric information. The monthly SST data are from the Hadley Center Sea Ice and SST monthly dataset (HadISST; Rayner et al. 2003), which is available for 1870–2021 and has a horizontal resolution of 1° × 1°. The monthly ocean potential temperature, ML depth, meridional flows, and zonal flows are from the NCEP Global Ocean Data Assimilation System (GODAS; Behringer and Xue 2004), which is available for 1980–2021 and has a latitude–longitude resolution of 0.333° × 1.0°. Previous studies have demonstrated that the temperature, thermocline depth, and ocean currents in this dataset, despite not being completely accurate, are remarkably close to actual observations (Huang et al. 2010; Nishida et al. 2011). Although there are biases, the GODAS heat budget analysis is very useful for monitoring and understanding the physical processes that control temperature changes at the sea surface. For the atmospheric information, monthly geopotential height, sea level pressure (SLP), surface zonal wind, surface meridional wind, latent heat fluxes, sensible heat fluxes, net shortwave radiation, and net longwave radiation at the sea surface are from the NCEP–NCAR Reanalysis 1 dataset (Reanalysis 1; Kalnay et al. 1996), which is available for 1948–2021 and has a horizontal resolution of 2.5° × 2.5°. We also used monthly atmospheric information provided by the Twentieth Century Reanalysis (V2) dataset (20CRV2; Compo et al. 2011) from NOAA's Cooperative Institute for Research in Environmental Sciences (CIRES), which is available for 1871–2012 and has a horizontal resolution of 2° × 2° and 24 pressure levels.

Two analysis periods were used in this study due to the different available periods of atmospheric and oceanic datasets. A long period (1871–2021) was used for most MHW analyses, whereas a short period (1980–2021) was used for analyzing the ocean ML heat budget. For both periods, anomalies were defined as deviations from the 1981 to 2010 climatology after removing the linear trend throughout the analysis period. To obtain the atmospheric anomalies for the long period, we have to combine the 1871–1947 anomalies calculated from the 20CRV2 and the 1948–2021 anomalies calculated from the Reanalysis 1 using a two-dimensional cubic interpolation.

While the identification of MHWs generally relies on exceeding a critical value in total SST, the removal of the linear trend

in MHW analysis may not seem imperative. Nevertheless, our study primarily focuses on the interannual component of MHW SSTAs and their underlying generation mechanisms, necessitating the elimination of the linear trend to uncover the interannual SSTA component responsible for heatwave generation. Hence, in this study, we adhered to the guidance provided by Hobday et al. (2016) and defined MHW events by employing the 90th percentile threshold of SSTA indices calculated in the GOA or COJ regions over the period from 1981 to 2010. Following a similar methodology to Chen et al. (2021), we considered MHW events that exceeded the threshold for a minimum duration of 5 months, with intervals between events of no more than 1 month.

A wave activity flux (WAF) analysis was used to study Rossby wave activities induced by different variants of MHWs. The WAF vectors are parallel to the local group velocity of stationary Rossby waves under the Wentzel–Kramers–Brillouin approximation (Takaya and Nakamura 2001). In this study, only the horizontal components of this WAF are used, and the formula is calculated as follows:

$$\mathbf{W} = \frac{p\cos\varphi}{2|U|}\begin{Bmatrix} \dfrac{u}{a^2\cos\varphi^2}\left[\left(\dfrac{\partial\psi'}{\partial\lambda}\right)^2 - \psi'\dfrac{\partial^2\psi'}{\partial\lambda^2}\right] + \dfrac{v}{a^2\cos\varphi}\left[\dfrac{\partial\psi'}{\partial\lambda}\dfrac{\partial\psi'}{\partial\varphi} - \psi'\dfrac{\partial^2\psi'}{\partial\lambda\partial\varphi}\right] \\ \dfrac{u}{a^2\cos\varphi}\left[\dfrac{\partial\psi'}{\partial\lambda}\dfrac{\partial\psi'}{\partial\varphi} - \psi'\dfrac{\partial^2\psi'}{\partial\lambda\partial\varphi}\right] + \dfrac{v}{a^2}\left[\left(\dfrac{\partial\psi'}{\partial\varphi}\right)^2 - \psi'\dfrac{\partial^2\psi'}{\partial\varphi^2}\right] \end{Bmatrix}. \quad (1)$$

Here, p denotes the relative pressure, U denotes the basic state wind speed, (u, v) denotes the basic state wind, and ψ' denotes the perturbed streamfunction.

An ocean ML heat budget analysis was conducted using the equations following Cronin et al. (2013), which is expressed as

$$\frac{dT_m}{dt} = \frac{Q_{\text{net}} - Q_{pn}(h_m)}{\rho_0 c_p h_m} - \left(u_m\frac{\partial T_m}{\partial x} + v_m\frac{\partial T_m}{\partial y}\right) + \kappa\nabla^2 T_m - \frac{w_e\Delta T_m}{h_m}, \quad (2)$$

where T_m is the ML temperature, h_m is the ML depth, u_m is the ML zonal current velocity, v_m is the ML meridional current velocity, w_e is the vertical velocity at the ML bottom, κ is the eddy diffusivity, ρ_0 (1026 kg m^{-3}) is the reference density of seawater, and c_p (4200 J kg^{-1} K^{-1}) is the specific heat of seawater at constant pressure (Shi et al. 2017). Here, Q_{net} denotes the net surface heat flux, which is positive downward, and $Q_{pn}(h_m)$ is the downward radiative shortwave flux penetrating the ML, which is obtained from the following equation (Vijith et al. 2020):

$$Q_{pn}(h_m) = \alpha \text{SWR}_{\text{net}} e^{-\lambda h_m}. \quad (3)$$

Here, SWR_{net} is the sea surface net shortwave radiation, α is the sea surface albedo (0.38), and λ is the inverse of folding depth (20 m). In our heat budget calculations, all variables (i.e., ML temperature, depth, and current anomalies) are monthly varying local data. The third and fourth terms on the right-hand side of the equation in this study were combined into one as the oceanic process at the ML bottom.

3. A basinwide MHW "conditioning" mode in the North Pacific

We applied an EOF analysis to extract the leading variability modes of SST in the North Pacific between 17° and 60°N for both the long (1871–2021) and short (1980–2021) periods of the HadISST product. The first EOF (explained variance 32%; not shown), which is well known to be associated with Aleutian low variations (Deser and Blackmon 1995; Minobe and Mantua 1999), also called the Pacific decadal oscillation (PDO) (Mantua and Hare 2002), is not relevant to this study. As shown in Figs. 3a and 3b, a basinwide warming pattern appears in the second EOF model (EOF2) during both periods. SSTA structures of both EOF2 modes are characterized by a spread of warm SSTAs from the northeast (NE) Pacific near the GOA region to the northwest (NW) Pacific near the COJ region. Both show a tendency to have a primary warming center over the GOA and a secondary center over the COJ. This dual-center feature is particularly clear in the EOF2 mode calculated from the shorter 1980–2021 period (Fig. 3b). This feature suggests that this EOF2 mode of North Pacific warming can have a major center at the GOA or COJ region or both. Both the 2013–16 and 2018–22 MHWs can be a manifestation of this EOF2 mode, except that the 2013–16 event had more intensive warming in the GOA center than in the COJ center, whereas the 2018–22 event had two active warming centers in both the GOA and COJ. This suggestion is further supported by the fact that the principal components (PCs) of the two EOF2 modes (PC2 hereafter) consistently show large positive values during the periods when the 2013–16 and 2018–22 MHWs occurred (Fig. 3c). In a recent study, Werb and Rudnick (2023) highlighted the growing importance of the EOF2 mode in response to the recent occurrences of North Pacific MHWs. They pointed out that persistent MHW events in the North Pacific Ocean since 2014 have been shown to result in a gradual expansion of the positive lobe of EOF2 and an increasing significance of the EOF2 mode of North Pacific SST. Based on the EOF2 mode from the shorter 1980–2021 period, we used the SSTAs averaged within the GOA (160°–135°W, 37.5°–47.5°N) and COJ (155°E–180°, 37.5°–47.5°N) regions to define GOA and COJ indices for the analyses of the GOA and COJ MHW variants of the North Pacific basinwide mode.

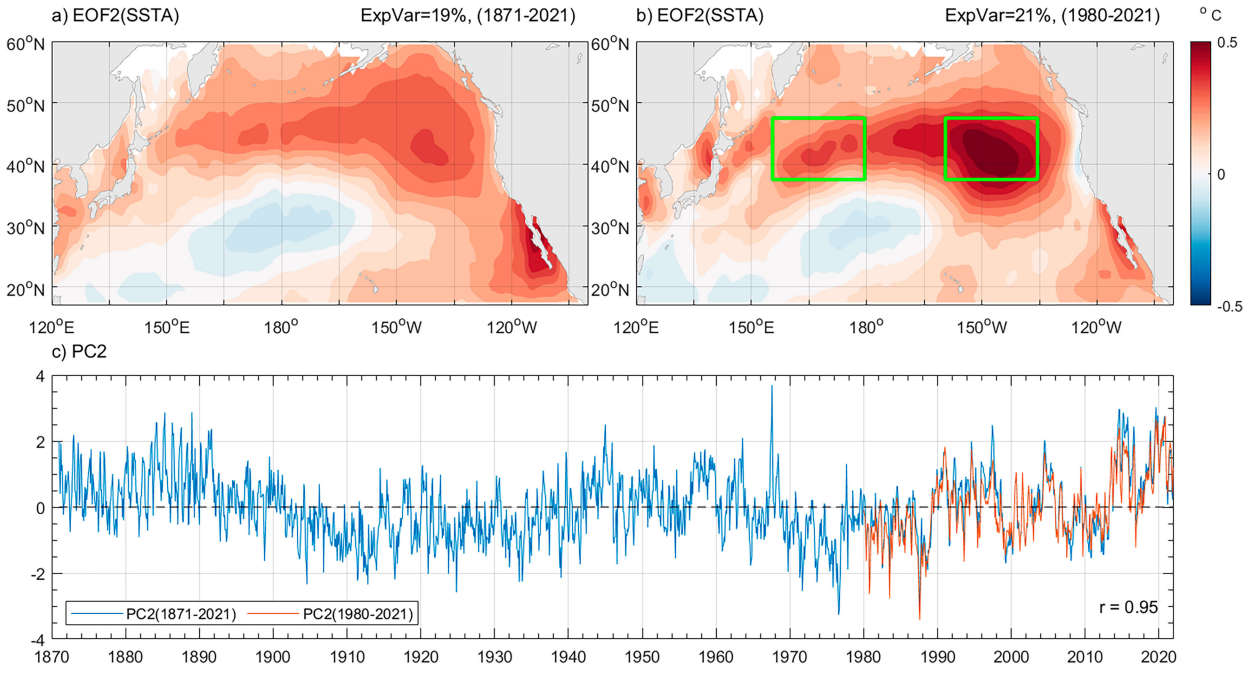

FIG. 3. The second EOF mode of SST variability in the North Pacific (between 17° and 60°N) during the periods (a) 1871–2021 and (b) 1980–2021. The percentages of total variance explained by each EOF mode (i.e., ExpVar) are shown. (c) The time series of their corresponding PC2 values during the two analysis periods. The PC2s have a correlation coefficient (r) of 0.95 during the sharing period. Green boxes in (b) indicate the regions where the GOA and COJ indices are defined.

In previous studies, the EOF2 mode was often referred to as the Victoria Mode and was often linked to interannual-to-interdecadal SST variability of the North Pacific climate (Bond et al. 2003), such as that associated with the North Pacific Gyre Oscillation (Di Lorenzo et al. 2008). Those earlier studies typically emphasized this EOF2 mode as having a northeast–southwest-oriented dipole pattern of SSTAs, which can be seen in Figs. 3a and 3b. However, the northern lobe of this so-called dipole structure has much larger loadings than the southern lobe. Also, the northern lobe has a basinwide structure across the entire North Pacific that is absent in the southern lobe. This basin structure of the EOF2 mode was not emphasized much in those earlier studies. In this study, we emphasize the basinwide characteristic rather than the meridional dipolar structure of the EOF2 mode as representing a basinwide mode in the North Pacific. The corresponding basinwide SST "condition" of this EOF2 mode can either favor or hinder the occurrence of North Pacific MHWs in the GOA or COJ regions during its positive or negative phase. When the "MHW conditioning" mode is in its positive phase, it creates favorable SST conditions that increase the likelihood of MHW events in these two regions. As depicted in Fig. 4, during the periods of the positive EOF2 mode, the frequency of MHW appearance in the GOA and COJ regions nearly doubles when compared to the frequency observed during the entire analysis period. In this analysis, the MHWs were identified using a threshold value defined by the 90th (Fig. 4a), 95th (Fig. 4b), or 99th (Fig. 4c) percentile of the

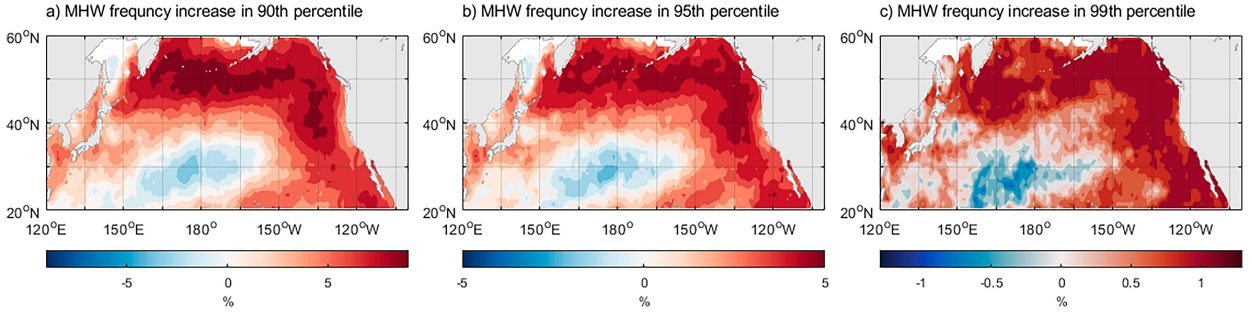

FIG. 4. Percentage (shading; %) of the MHW monthly frequency increase at different SSTA percentile thresholds during the EOF2 positive mode in comparison to the entire time period: (a) 90th, (b) 95th, and (c) 99th percentile.

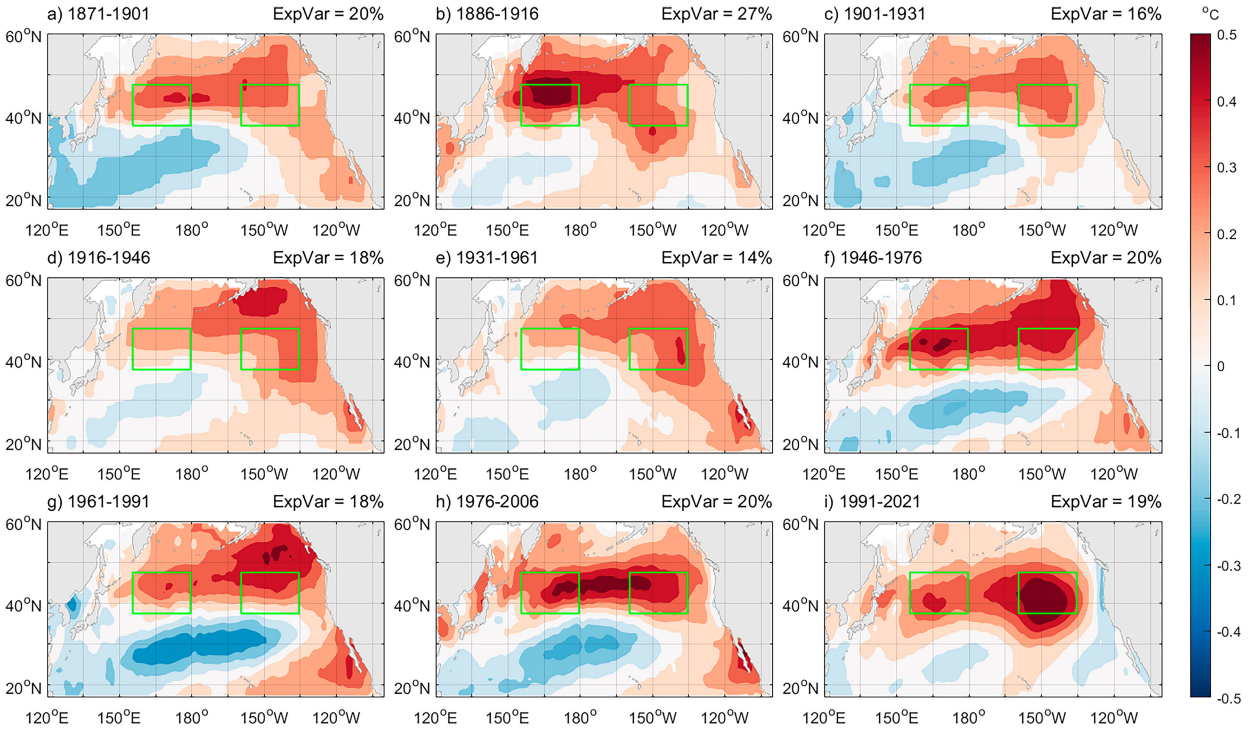

FIG. 5. The second EOF mode of SST variability in the North Pacific was obtained by applying the EOF analysis to nine 31-yr segments of SSTA data during 1871–2021 with a 15-yr gap between the segments. The percentage of total variation explained by the mode (i.e., ExpVar) is shown in each panel. Green boxes are the GOA and COJ regions defined in Fig. 3b.

entire dataset for each point of SSTA. If the SSTA for a given month exceeds the threshold, we categorize that month as an MHW month. We then calculated the frequency of MHW month for each point during the positive phase of the MHW conditioning mode and compared it to the frequency for the entire period. Regardless of the threshold used, the positive phase of the MHW conditioning mode consistently increases the frequency of MHW appearance in both the GOA and COJ regions. This compelling evidence indicates that the positive phase of the MHW conditioning mode significantly impacts the frequency of MHW month in the North Pacific's GOA and COJ regions, emphasizing its role in shaping the dynamics of these MHW variants.

To further examine the existence of the double-center feature of this North Pacific MHW conditioning mode, we conducted a separate EOF analysis for nine 31-yr segments of the SST data from 1871 to 2021, with a 15-yr gap between the segments (Fig. 5). Interestingly, the warming center of the mode alternates between the GOA and COJ regions from segment to segment during the past about 150 (i.e., 1871–2021) years. The basinwide warming mode has only one major center over the GOA during the 1916–46 and 1931–61 segments (Figs. 5d,e), only one major center over the COJ during the 1886–1916 segment (Fig. 5b), and two centers over both the GOA and COJ during the 1901–31, 1946–76, 1961–91, 1976–2006, and 1991–2021 segments (Figs. 5a,c,f–i). This segment EOF analysis confirms that the Pacific MHW conditioning mode has two preferred warming centers and can alternate between a variant that has a warming center over the GOA and a variant that has a warming center over the COJ.

The power spectrum of the PC2 from the 1871 to 2021 period (Fig. 6a) shows that, compared to the red noise spectrum, this North Pacific MHW conditioning mode has distinct spectral peaks in three frequency bands: one in the decadal band (>10 years), one in the interannual band (3–7 years), and one in the high-frequency band (around 12 months). While the decadal and interannual bands are known to separately relate to the North Pacific Gyre Oscillation and El Niño–Southern Oscillation based on previous studies (e.g., Bond et al. 2003; Di Lorenzo et al. 2008; Ding et al. 2015), the high-frequency band of this EOF2 mode represents basinwide activities of high-temperature events, especially the intra-annual portion. In Fig. 6b, we examined the probability density function of the warming duration of the PC2 for the period 1871–2021. Here, the event's duration is defined as the time when the PC2 stayed above its 90th percentile (0.898 standard deviation of the whole period) calculated from the 1981 to 2010 period (i.e., the period we used to define atmospheric and oceanic climatologies). We find that the duration shows a bimodal distribution, with the largest peak in the shortest 1–2-month range and a second distinct peak in the 5–10-month range. The second peak of the probability density function is close to the high-frequency peak of the power spectrum shown in Fig. 6a. Therefore, the high-frequency portion of the EOF2 pattern particularly relates to North Pacific MHW activities.

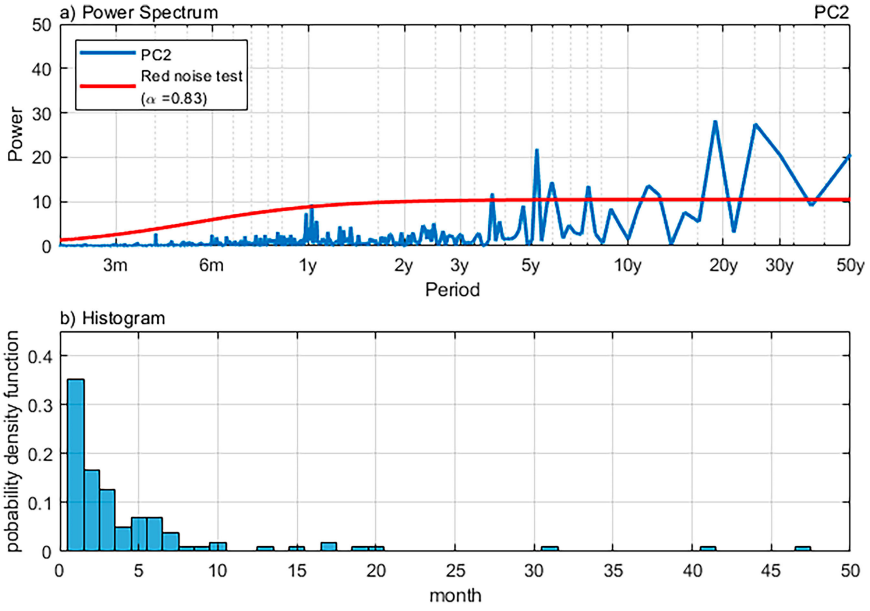

FIG. 6. (a) The power spectrum of PC2 (blue line) during 1871–2021 and (b) the probability density function of the duration of the high-temperature events identified based on the PC2. The duration is determined as the time during which the PC2 values stay above the 90th percentile of the PC2 values. The 90th percentile is defined based on the PC2 values in 1981–2010 where the atmospheric and oceanic climatology is calculated in this study. In (a), the red noise spectrum (red line) is constructed based on a 1-month lag autocorrelation coefficient of 0.83, as shown in the legend.

4. Driving mechanisms of the Pacific MHW conditioning mode and its two variants

a. Associated atmospheric circulation patterns

The Z200 can display the wave train structure of the atmosphere more clearly, due to the equivalent barotropic structures of atmospheric wave trains. We regressed the anomalies of Z200 for the long 1871–2021 period to examine the atmospheric circulation pattern associated with the Pacific MHW conditioning mode and its two favorable MHW variants. Performing regression/correlation analyses on the PC2 allows us to accurately discern the essential characteristics shared by the GOA and COJ variants of MHWs. Additionally, by conducting similar analyses on both the GOA and COJ indices, we can pinpoint significant differences, such as divergent wave propagation paths, that distinguish the GOA and COJ variants from each other. The PC2-regressed Z200 anomalies (Fig. 7a; contours) have positive values spanning over the North Pacific with two separated centers over the NE (around 60°N, 120°W) and NW Pacific (around 40°N, 120°W). The SST warming center in the GOA region is located on the southern flank of the NE Pacific high anomaly, while the COJ warming center is located to the east of the NW Pacific high anomaly. Similar Z200 anomalies are seen in the regressions to the GOA and COJ indices, except that the anomalous high intensified over the NE Pacific for the GOA variant (Fig. 7b) but intensified over the NW Pacific for the COJ variant (Fig. 7c). These regression analyses suggest that both the GOA and COJ warmings can be explained as thermodynamic responses to atmospheric high anomalies overhead.

Liang et al. (2017) argued that the anomalous high pressure over the GOA during the 2013–15 Pacific Blob (i.e., the GOA variant of the MHW conditioning mode discussed here) is part of a hemispherical circulation pattern that spans over the North Pacific, North America, and North Atlantic with a barotropic structure. The anomalous circulation in the upper troposphere is characterized by a wave train pattern over the Pacific and North American sectors and a zonal flow vacillation pattern over the Atlantic sector (see their Fig. 2a). These two characteristics can be identified in the Z200 anomaly regression to the PC2 (and GOA) (Figs. 7a,b). However, we notice that there appears to be one major wave train pattern emanating from the tropical central Pacific and one minor wave train pattern emanating from the tropical western Pacific in the PC2 regression. The two wave train features are even more evident when we conducted the regression only for the boreal winter [December–February (DJF)] season (Fig. 7d). It is well known that the atmosphere is barotropically more unstable during winter than the other three seasons and is more capable of producing wave trains (Simmons et al. 1983). The major wave train, after emanating from the tropical central Pacific, passes through the subtropical central Pacific near Hawaii (20°N, 165°W), the North Pacific with an anomalous center around 175°W and 40°N, and the North American coast near Alaska (60°N, 160°W) and then curves southward through Canada to the southeastern United States.

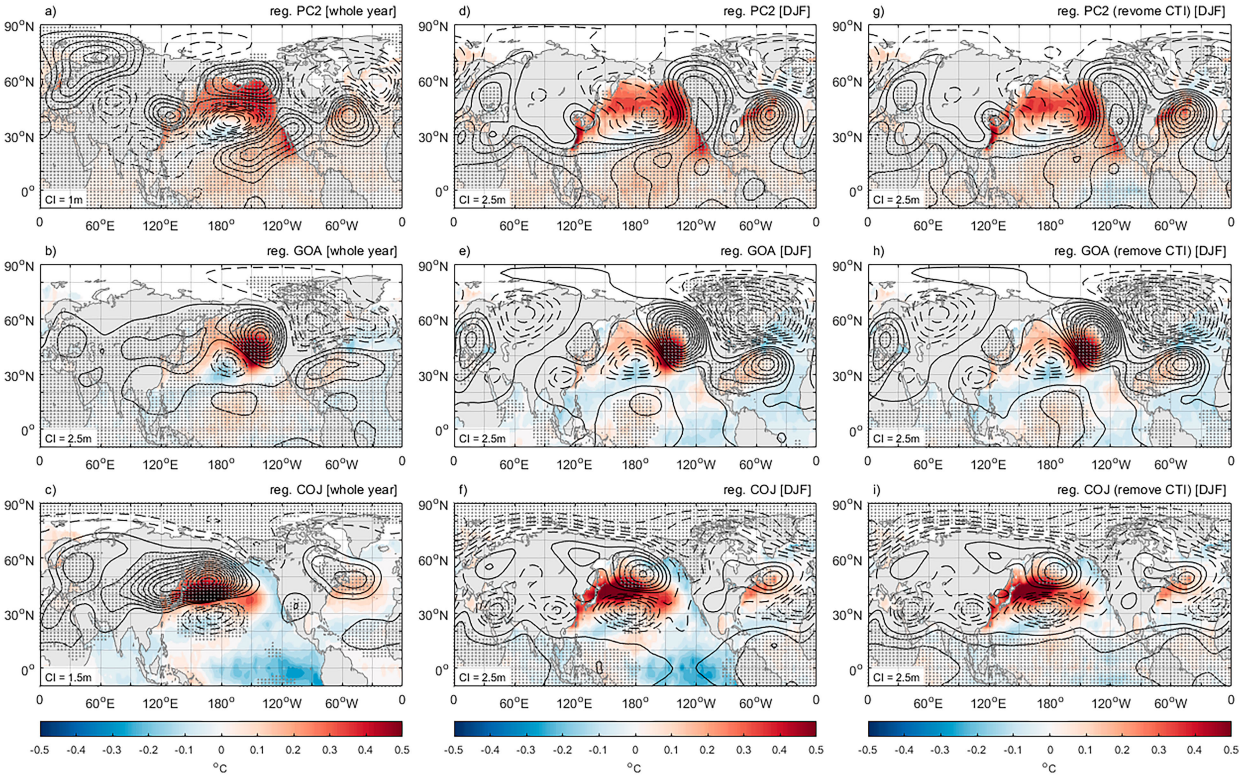

FIG. 7. (a)–(c)Anomalies of Z200 (contours; m) and SST (shadings; °C) regressed onto (top) the PC2, (middle) the GOA index, and (bottom) the COJ index during the period 1871–2021 using all calendar months. (d)–(f) As in (a)–(c), but calculated using only the anomalies averaged from the winter months (December– February). (g)–(i) As in (d)–(f), but calculated with the residual Z200 and SSTAs after removing their regressions onto the cold tongue index (CTI). The gray dotted area is consistent with representing the 95% confidence level of Z200, and contour intervals are labeled.

The anomalous high center over Alaska is responsible for providing the atmospheric forcing to drive the GOA warming center. The second minor wave train, after emanating from the tropical western Pacific, passes through the subtropical northwestern Pacific (30°N, 120°E), Japan, and Siberia (40°N, 125°E) and finally curves southeastward through North America. The anomalous high center over Japan and Siberia is responsible for providing the atmospheric forcing to drive the COJ warming center. The Z200 regressions over the North Atlantic are dominated by a north–south dipolar structure, similar to the zonal flow vacillation mentioned in Liang et al. (2017). This north–south zonal dipolar pattern is also more evident in the DJF regression (e.g., Fig. 7d). In other seasons (spring, summer, and fall), although the intensity of the Z200 anomalies varies (Fig. S1 in the online supplemental material), the main structure of the regression pattern (i.e., the characteristics of the North Pacific–North American wave train propagation features and the North Atlantic zonal vacillation) remains unchanged.

The Z200 regressions onto the GOA and COJ indices produce similar wave train patterns over the Pacific and similar north–south zonal flow patterns over the North Atlantic but with two interesting and important differences. First, the Pacific wave train is more dominated by a path emanating from the tropical central Pacific in the regression to the GOA index (Fig. 7b) but more dominated by a path emanating from the tropical western Pacific in the regression to the COJ index (Fig. 7c). Both wave train patterns and paths and their different tropical origins seen in GOA and COJ regressions can be found in the PC2 regressions (Fig. 7a). Consistently, a strong anomalous high is produced over Alaska in the GOA-index regression and over Japan in the COJ-index regression and is, respectively, responsible for driving the GOA and COJ warming centers. The different wave train paths between these two variants are particularly clear during the DJF (Figs. 7d–f) regressions. The second difference between the GOA- and COJ-index regressions appears over the North Atlantic, where the north–south zonal flow dipolar pattern switches the polarity between these two regressions. While the north–south pattern in the GOA-index regression (Fig. 7b) is dominated by a negative anomaly center in the subpolar region of the North Atlantic (around 60°N) and a positive anomaly center in the subtropics (around 30°N), the north–south pattern in the COJ-index regression (Fig. 7c) is dominated by a positive Z200 anomaly center in the midlatitudes of the North Atlantic (around 45°N) and negative anomaly centers to the north and south. To ensure that these two differences between the GOA- and COJ-index repressions are not caused by the possible

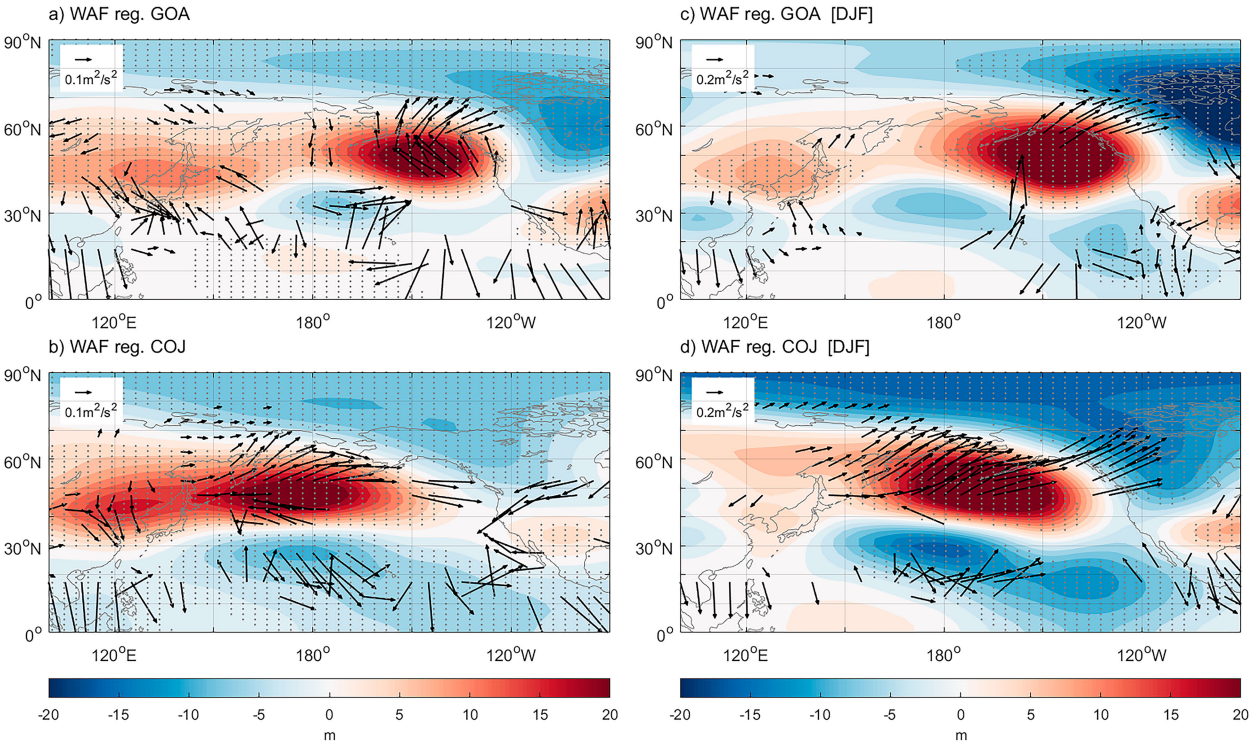

FIG. 8. (a)–(c) Anomalies of wave activity flux (WAF) (vectors; $m^2\ s^{-2}$) and anomalies of Z200 (shadings; m) regressed onto the (top) GOA index and (bottom) COJ index during the period 1871–2021 using all calendar months. (d)–(f) As in (a)–(c), but calculated using only the anomalies averaged from the winter months (December–February). The WAF is shown only when the zonal or meridional component is significant at the 95% confidence level. The gray dotted area is consistent with representing the 95% confidence level of Z200.

different ENSO conditions in the tropical Pacific, we repeated the DJF regression analyses but with the residual Z200 anomalies and SSTAs after their linear regressions onto the cold tongue index (CTI) were removed. Here, the CTI is defined as the SSTAs averaged over the tropical Pacific within 6°N–6°S and 180°–90°W. Similar Z200 regressions are seen (Figs. 7g–i) with and without the CTI regressions removed, indicating that the differences between the GOA- and COJ-index regressions are not related to ENSO conditions.

We conducted a WAF analysis to further validate the propagation paths of the two MHW variants, which capture wave propagation. The results, presented in Fig. 8, show the horizontal components of the 200-hPa WAF anomalies regressed on the GOA and COJ indices. Regarding the GOA variant, our findings indicate that its wave train originates in the tropical mid-Pacific Ocean, approximately at 160°W. Subsequently, it travels toward the Aleutian Islands and the GOA region, playing a crucial role in the MHW occurrences in these areas. On the other hand, the wave train associated with the COJ variant originates in the tropical western Pacific Ocean, at around 160°E. It then propagates along the western Pacific Ocean toward higher latitudes, passing through the COJ region and exhibiting a significant turning pattern. The WAF analysis has also detected another WAF component within the COJ variant, which migrates from Eurasia to the NW Pacific. This particular component might also play a role in the development of the COJ variant.

Our analyses here suggest that 1) the Pacific MHW conditioning mode is a North Pacific local response to a hemispheric-scale atmospheric circulation anomaly spanning over the North Pacific and Atlantic sectors, 2) both of the variants are driven by an atmospheric wave train mechanism over the North Pacific but with two different preferred propagation pathways, 3) whether this MHW conditioning mode should favor the occurrence of the GOA or COJ variants or both depends on the relative strengths of the two Pacific wave train paths of this circulation pattern, and 4) the GOA and COJ MHW variants are accompanied by different phases of atmospheric circulation patterns over the North Atlantic, raising the possibility of being accompanied by different patterns of North Atlantic SSTAs.

b. *Properties of the two variants in ocean ML*

Before further exploring the possible Atlantic associations between the GOA and COJ variants induced by the Pacific MHW conditioning mode, we need to confirm that these two variants are truly thermodynamically driven by the atmosphere. Equation (2) expresses the synthetic term of the ML temperature tendency and therefore corresponds to the tendency of the MHW index, and therefore, the individual terms

of the ocean ML heat budget in this study are regressed on the time derivatives of the PC2, GOA index, and COJ index.

The regression of the time tendency term of the ML temperature to the PC2 (Fig. 9d) resembles the SSTA structure of the EOF2 mode (Fig. 9a), except that the double-center feature is more apparent in the ML tendency regression than in the SSTA structure. Similarly, the ML tendency regressions to the GOA and COJ indices (Figs. 9e,f) resemble the SSTA structures regressed onto the two indices (Figs. 9b,c), although the SSTAs and ML ocean temperature tendencies of the GOA and COJ variants exhibit different centers of maximum warming. The warming of both variants spreads to the other side of the North Pacific, exhibiting a basinwide warming signature similar to the SSTAs and ML temperature tendency of the EOF2 mode. Of the five driving terms on the right-hand side of the ML budget equation, the contribution of the surface heat flux term (Figs. 9g–i) is larger than that of all other oceanic process terms (Figs. 9j–o). The center of surface heat flux heating (i.e., reducing heat flux loss from the ocean surface) overlaps with the warming center of the ML temperature tendency anomaly for the MHW conditioning model and its two variants. The oceanic zonal advection term (Figs. 9j–l) is not important for the generation of the mode and its two variants, while the meridional oceanic advection term (Figs. 9m–o) is the second largest contributor to ML temperature warming. Figure 10 shows the SLP and surface winds anomalies regressed onto the PC2, GOA index, and COJ index. These patterns serve to confirm that the PC2, GOA, and COJ MHW variants are accompanied by a positive SLP anomaly center overhead (Figs. 10a–c), as well as anomalous anticyclonic surface winds. The presence of a positive SLP anomaly can contribute to net surface heat flux anomalies. We also conducted similar regression analyses with the four components of the surface heat flux term and found that the latent heat flux (Fig. S2) is the most important component to provide the surface heat flux warming to the MHW conditioning mode and the two variants of MHW. It is followed by the sensible heat flux and net longwave radiative flux, both of which provide positive contributions to the net surface heat flux forcing the MHW generation. The anomalous anticyclonic surface winds, consistent with the SLP anomaly, exhibit a southern branch, weakening the midlatitude westerlies and contributing to positive latent heat flux anomalies. Ge et al. (2023) suggested that the meridional wind component can also contribute to positive latent heat flux anomalies by transporting moisture from lower latitudes. This, in turn, reduces evaporation over the MHW region. The zonal wind anomalies associated with the anomalous SLP high can produce an anomaly of ocean advection to the north, bringing warmer seawater to the north, and leading to the transport of warmer seawater to the north and causing meridional ocean advection along 40°N, contributing positively to the warming. These findings align with previous studies (e.g., Liang et al. 2017) concerning the Pacific Warm Blob, which closely resembles our GOA variant of the MHW Pacific. The contribution of the meridional advection term is about 20% of the contribution of the heat flux term. Vertical advection and diffusion contributions are combined and calculated as the residual term of the budget equation (Figs. 9p–r). This term contributes significantly to the ML heat budget but behaves as a cooling effect and is more likely to act as the primary mechanism for suppressing or even terminating heatwave events.

For the sensible heat flux term (Figs. S2d–f), high pressure blocking anomalies in the atmosphere increase surface air temperature and warm air brings positive anomalies in sea surface sensible heat fluxes. For the net longwave radiative flux term (Figs. S2j–m), contrary to common belief, our results suggest that the total cloud cover within the region of the heating center increases (Fig. S3), greatly impeding the upgoing longwave radiation. This hindrance to the propagation of longwave radiation leads to positive anomalies in sea surface heat flux, ultimately contributing to the growth of the MHW. Some other previous studies (Schmeisser et al. 2019; Kuroda and Setou 2021) also pointed out the longwave radiation anomaly has contributed to the formation of MHW, which supports our work. The increased cloud cover observed during MHWs is associated with high clouds rather than low clouds, as emphasized by Schmeisser et al. (2019). This elevated high cloud presence is likely a result of the elevated SSTAs associated with the heatwave, which can foster atmospheric instability, creating conditions conducive to the formation of high clouds. Only the net shortwave flux (Figs. S2g–i) contributes to the termination of the MHW. Our ML heat budget analyses suggest that the Pacific MHW conditioning mode and the associated two MHW variants are driven primarily by atmospheric heat fluxes and damped by ocean vertical processes.

c. *Linkages with the North Atlantic*

As mentioned, the GOA and COJ variants of MHW induced by the MHW conditioning mode are accompanied by different Z200 anomaly structures in the North Atlantic region. The north–south pattern of the GOA variant (Fig. 7b) is dominated by a negative anomaly center in the middle-to-high latitudes of the North Atlantic and a positive anomaly center in the subtropics (around 30°N), while the north–south pattern of the COJ variant (Fig. 7c) is dominated by a positive Z200 anomaly center in the midlatitudes of the North Atlantic (around 45°N) and negative anomaly centers in the north and south. Corresponding to the different Z200 anomaly patterns, we also find that opposite phases of tripolar SSTA patterns occur in the North Atlantic between these two variants (see Fig. 7). The tripolar pattern in the GOA variant has a warm anomaly center in the subtropical Atlantic (around 30°N) and two cold anomaly centers in the subpolar and subtropical Atlantic (Fig. 7b). In the COJ variant (Fig. 7c), a roughly reversed phase of the tripolar pattern appears in the North Atlantic. A cold anomaly center in the subtropical Atlantic Ocean (around 20°–30°N) is juxtaposed with warm anomaly centers in the north and south (Fig. 7c). The difference in this tripolar SSTA pattern is more pronounced when the GOA- and COJ-index regressions were performed during the winter season (see Figs. 7e,f). As shown in Figs. 7g–i, the GOA and COJ variants still show opposite phases of tripolar patterns of SSTA in the North Atlantic after the CTI regression is

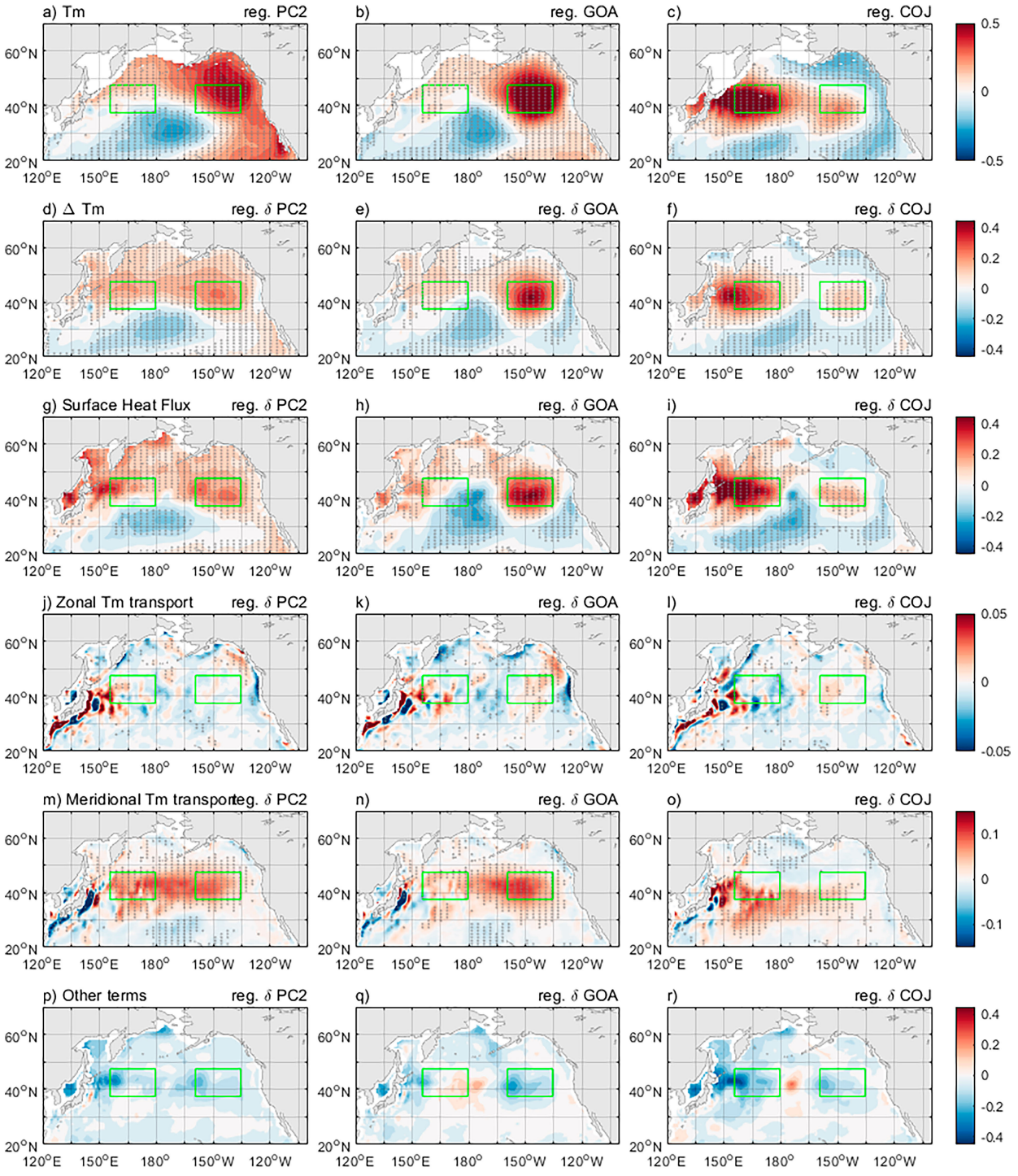

FIG. 9. Regressions of mixed layer temperature (T_m; °C) anomalies onto (a) the 3-month running mean PC2, (b) the GOA index, and (c) the COJ index. The remaining five rows show the regressions of the ML heat budget terms (°C) onto the time tendency of (left) the PC2 (δPC2), (center) the GOA index (δGOA), and (right) the COJ index (δCOJ), which include (d)–(f) the time tendency term of ML temperature, (j)–(l) the zonal ocean advection term, (m)–(o) the meridional ocean advection term, and (p)–(r) the residual term (i.e., the combination of the vertical advection and diffusion terms). The calculations were performed for the period 1980–2021. The gray dotted area (except for the last row) is consistent with representing the 95% confidence level, and green boxes mark the GOA and COJ regions.

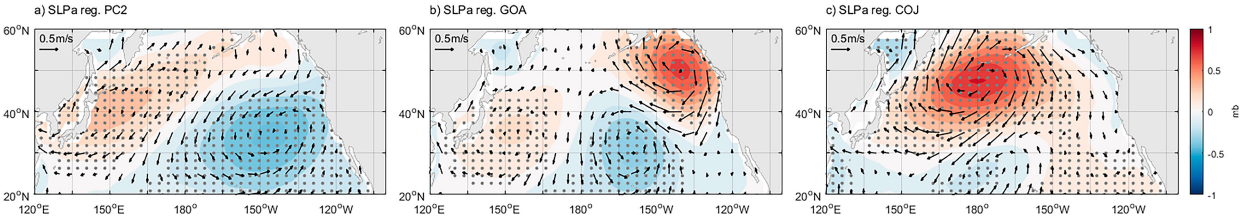

FIG. 10. Anomalies of sea level pressure (SLP; mb; shadings; 1 mb = 1 hPa) and surface wind (vectors; m s^{-1}) regressed onto the (a) PC2, (b) GOA index, and (c) COJ index during the period 1871–2021. The gray dotted area is consistent with representing the 95% confidence level of Z200, and contour intervals are labeled. The gray dotted area is consistent with representing the 95% confidence level.

removed. To quantify and visualize this difference, we compare in Fig. 10 the meridional profiles of the zonal mean (averaged between 80° and 10°W) of SSTA regressions onto the PC2 (yellow), GOA index (orange), and COJ index (blue). No matter whether the regressions were performed with all-year anomalies (Fig. 11a), only the DJF anomalies (Fig. 11b), or the DJF residual anomalies (Fig. 11c), the GOA variant is always accompanied by a cold–warm–cold phase of the tripolar pattern from the subtropical to subpolar Atlantic, while the COJ variant is accompanied by a warm–cold–warm phase of the tripolar pattern although the tripolar centers do not correspond perfectly in latitude.

To further verify that the North Pacific and North Atlantic SSTAs are linked, we performed a singular value decomposition (SVD) analysis to identify the covarying SSTA pattern between the North Pacific and North Atlantic. The third leading SVD mode is shown in Fig. 12. The SST warming linked to the COJ variant corresponds to a meridional warm–cold–warm pattern in the North Atlantic. On the other hand, the SSTA associated with the GOA variant corresponds to a cold–warm–cold pattern in the North Atlantic (opposite phase to Fig. 12), which is consistent with our conclusion above.

It is well established that the tripolar SSTA pattern in the North Atlantic can be influenced by the meridional displacement of the tropospheric jet (Rodwell and Folland 2002; Hall et al. 2015; Nie et al. 2019), which is often referred to as the North Atlantic Oscillation (NAO; Barnston and Livezey 1987; Hurrell et al. 2003). The opposite phase of the tripolar SSTA patterns in the North Atlantic between the GOA and COJ variants is consistent with the north–south dipole of the Z200 anomaly pattern we discussed earlier. The north–south dipoles of the Z200 anomalies are influenced by the displacement of the tropospheric jet stream, with the high pressure anomaly at around 40°N and the low pressure anomaly at around 60°N, in association with the NAO.

It is possible that different SSTA conditions in the Atlantic Ocean affect the North Pacific through different mechanisms of interbasin associations (Lyu and Yu 2017; Sun et al. 2017), which may influence the duration of the Pacific MHW and develop feedback loops. More comprehensive research is needed to explore the potential role of interbasin associations in determining the duration of the Pacific MHW pattern. However, our analysis of the occurrence frequency of Pacific MHW events and the phase of the Atlantic multidecadal oscillation (AMO) from 1871 to 2021 suggests that Atlantic

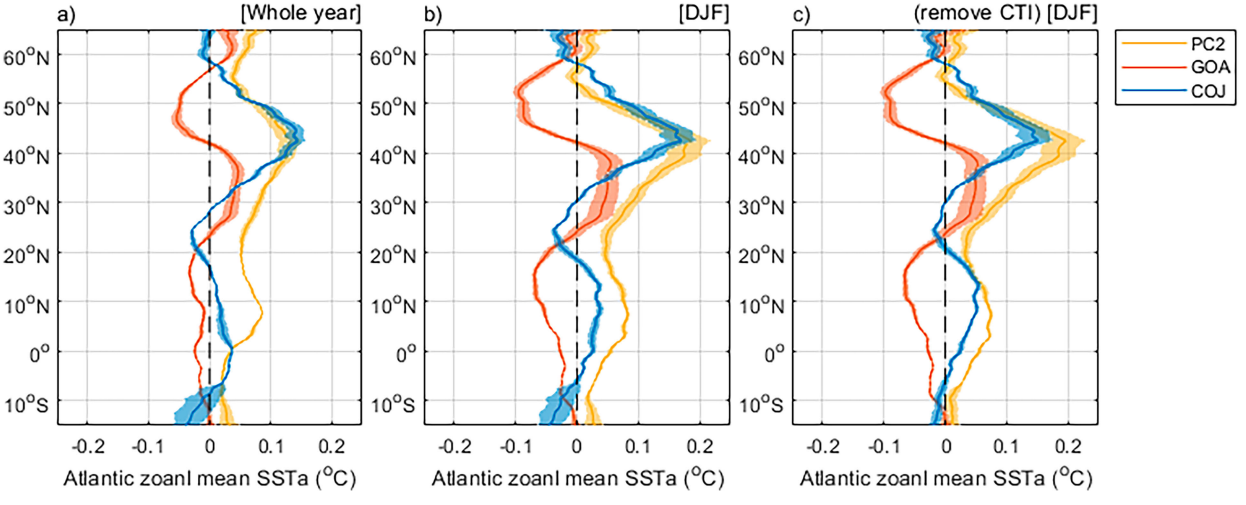

FIG. 11. Atlantic zonal-mean (averaged between 80° and 10°W) values of SSTA regressions onto the PC2 (yellow), GOA index (orange), and COJ index (blue) using (a) all calendar months, (b) only the winter DJF months, and (c) only the winter months and with the CTI effect removed; shading shows the 95% confidence interval using Student's *t* test.

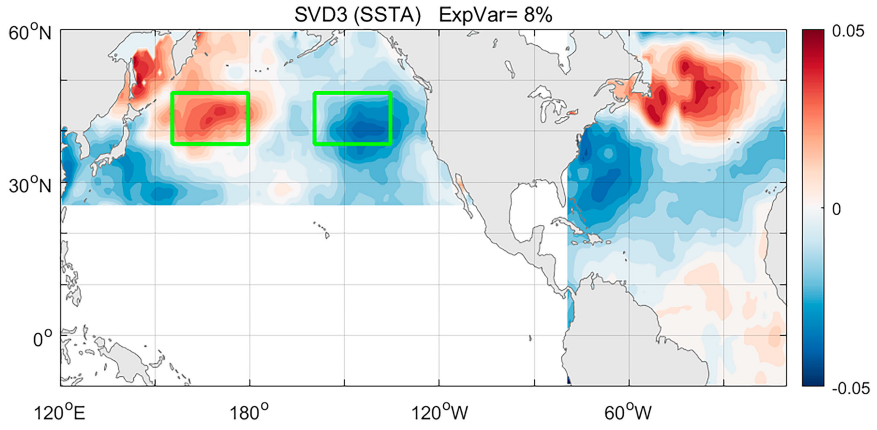

FIG. 12. The third singular value decomposition (SVD3) mode of the SSTAs in the North Pacific (120°E–100°W, 25.5°–60°N) and SSTAs in the North Atlantic (80°–10°W, 10°S–60°N) during the period 1871–2021. The percentages of total variance explained by the mode (i.e., ExpVar) are shown.

SSTs could potentially play a controlling role in Pacific MHW events. The AMO index is defined as the North Atlantic region's weighted average of 121-month low-pass filtered SSTAs between 0° and 70°N. In this analysis, we classify the "MHW" events identified by the PC2 as "high-temperature events." This terminology is employed because the identification relies on a time series generated from an EOF analysis, rather than utilizing actual SST or SSTA values. On the other hand, the events identified by the GOA and COJ indices continue to be referred to as MHW events. To detect these events, we set a threshold equivalent to the 90th percentile across the entire analysis period. Specifically, the threshold corresponds to 0.898 standard deviations for the PC2, 1.02 standard deviations for the GOA index, and 0.655 standard deviations for the COJ index. The identified events are indicated in Fig. 13. The result reveals that the high-temperature events and corresponding MHW events, including both the GOA and COJ variants, tend to occur more frequently during periods of the positive AMO phase (such as from the 1870s to 1900s and from the 1920s to 1960s) but less frequently during the negative AMO phase (such as from the 1900s to 1920s and from the 1960s to 1990s). Since the 1990s, the AMO has entered a positive phase, and the recent consecutive basin-wide MHW events in 2013–16 and 2018–22 suggest that more active MHW events may occur in the coming decades. However, further in-depth analysis is necessary to establish causality. Our results suggest that interbasin associations between the North Pacific and Atlantic are essential for comprehending the Pacific MHW events' characteristics.

5. Historical events of the two variants of the Pacific MHW conditioning mode

Our analysis over the past 151 years (i.e., 1871–2021) identified 27 Pacific high-temperature events based on the PC2 (Fig. 13a), 24 MHW events of the GOA variant based on the GOA index (Fig. 13b), and 35 MHW events of the COJ variant based on the COJ index (Fig. 13c). We compiled a comprehensive list of all these events in Tables 1–3 in the online supplemental material, which includes their start date, end date, duration, and normalized intensity. Additionally, we conducted case studies on two multiyear MHW events, the 2013–16 MHW and the 1955–58 MHW, to investigate whether their associated atmospheric circulation patterns and North Atlantic SST conditions align with the key features identified in our regression analyses.

The 2013–16 MHW is a clear example of the GOA variant of MHW, with most of the warming concentrated in the GOA region (Fig. 1a). We analyzed the atmospheric and oceanic anomalies during two subperiods of this event, which we have termed the GOA (i) and GOA (ii) periods (indicated by green dashed-line boxes in Fig. 1a). The GOA (i) period is characterized by significant GOA warming and some warming in the COJ region, albeit minimal. In contrast, the GOA (ii) period had only GOA warming. Figures 14a and 14b reveal that the Z200 anomalies averaged across both subperiods show a wave train pattern emanating from the tropical central Pacific. However, in the GOA (i) subperiod (Fig. 14a), a secondary wave train also emerges from the tropical western Pacific, consistent with the fact that this subperiod resulted in weak warming in the COJ region. Across the North Atlantic, both GOA (i) and GOA (ii) are accompanied by a positive phase NAO in Z200 anomalies, characterized by a high pressure anomaly over the Azores and a low pressure anomaly at 60°N over Iceland, and a cold–warm–cold phase of the tripolar pattern in SSTAs. All the atmospheric and oceanic anomaly features observed in this 2013–16 event align with our regression and correlation results. We should note that the zonal-mean values of Z200 were removed from the anomalies in Fig. 14 to better reveal wave train patterns in this case study.

The 1955–58 MHW (Fig. 15a) had its primary warming center located over the COJ region from mid-1955 to fall 1956 [COJ (i)] and then shifted to the GOA region [GOA (ii)]. The SSTAs in the midlatitude North Atlantic (Fig. 15b) switched from warm anomalies during COJ (i) to cold anomalies during

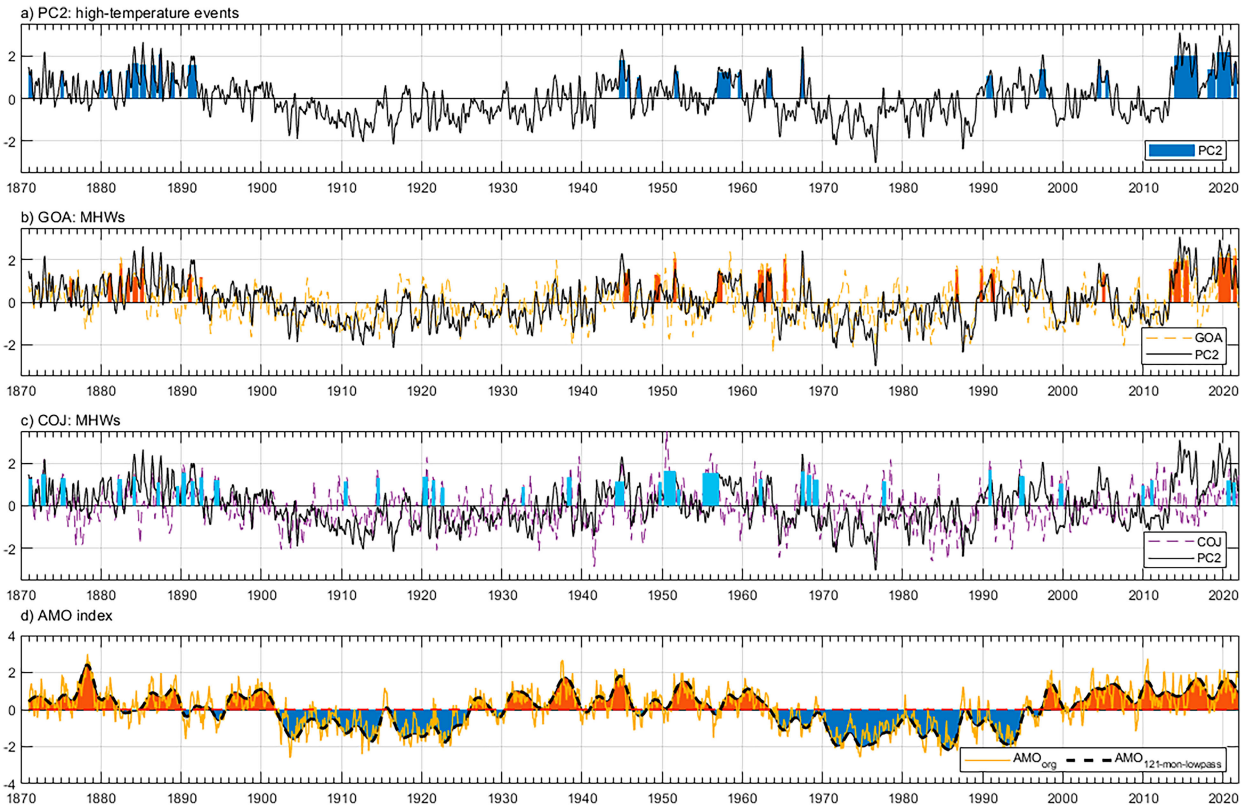

FIG. 13. Events (bars) of (a) Pacific high temperature and its (b) GOA variant and (c) COJ variant MHWs during 1871–2021, superimposed with the 3-month running mean of the corresponding PC2, GOA, and COJ indices; bar heights correspond to the normalized intensity of the periods. (d) The monthly AMO index (yellow line) and its 121-month low-pass filtered values (black-dashed line) during 1871–2021.

GOA (ii) in correspondence with the shift of the Pacific warming center. The event features a single warming center throughout its duration, with the warming center initially located in the COJ region during the first half of the event and shifting to the GOA region in the second half of the period, making it useful for studying atmospheric wave train paths when the single warming center is located in the different regions. During COJ (i), our analysis found that the Z200 anomalies (with the zonal mean removed) were primarily dominated by a wave train emanating from the tropical western Pacific over the North Pacific sector and a north–south vacillation of the jet stream (i.e., displacements of the Icelandic low or Azores high) over the North Atlantic sector. The North Atlantic SSTAs also displayed a warm–cold–warm tripolar pattern consistent with the COJ composite results (Fig. 15c). In contrast, the Z200 anomalies averaged over the

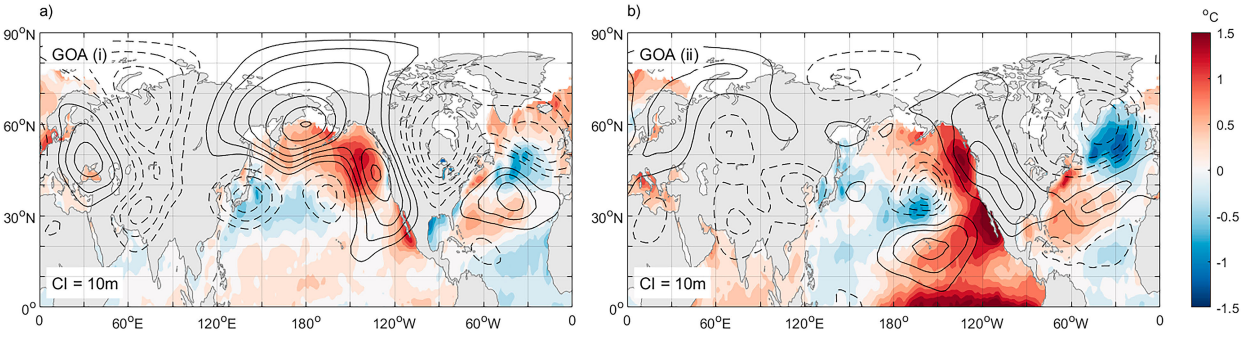

FIG. 14. Anomalies of SST (shading; °C) and Z200 (contours; m) averaged over (a) the GOA (i) subperiod and (b) the GOA (ii) subperiod of the 2013–16 MHW event in Fig. 1a. Contour intervals are 10 m. The zonal-mean values of Z200 were removed from the anomalies to better reveal wave train patterns in this case study.

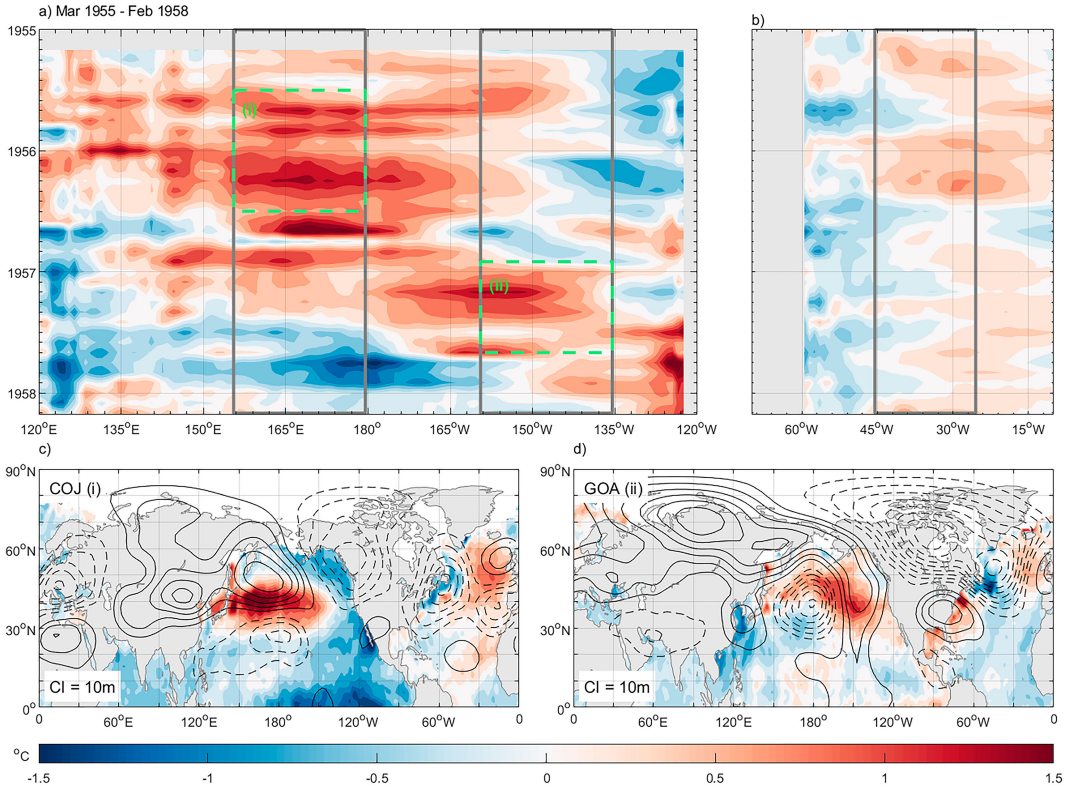

FIG. 15. Evolution of SSTAs during the 1955–58 MHW in (a) the North Pacific (averaged between 37.5° and 47.5°N) and (b) North Atlantic (averaged between 50° and 60°N). The green-dashed boxes in (a) represent the COJ (i) (July 1955–June 1956) and GOA (ii) (January–September 1957) subperiod examined in (c) and (d). (c),(d) The anomalies of SST (shadings; °C) and Z200 (contours; m) averaged over the COJ (i) and the GOA (ii) subperiods, respectively. Contour intervals are 10 m. The zonal-mean values of Z200 were removed from the anomalies shown in (c) and (d) to better reveal wave train patterns in this case study.

GOA (ii) subperiod exhibited a Pacific wave train emanating from the tropical central Pacific and a positive phase of NAO over the Atlantic (Fig. 15d). The SSTA pattern in the North Atlantic showed a cold–warm–cold pattern from the subpolar to subtropical regions, which is also consistent with our regression results.

6. Discussion

This study presents observational analyses suggesting that the 2013–16 and 2018–22 MHW events in the North Pacific are two different variants induced by a basinwide MHW conditioning mode. Each variant is driven by one of the two distinct atmospheric wave train patterns observed in the conditioning mode. However, these two patterns follow different propagation paths. The GOA variant is induced by the wave train emanating from the tropical central Pacific, while the COJ variant is induced by the wave train emanating from the tropical western Pacific. Our study suggests that a cluster of North Pacific MHW events is associated with a specific (or anomalous) atmospheric circulation pattern characterized by a wavelike pattern extending from the tropical Pacific to the North Pacific and from the North Pacific to the North Atlantic. These two variants of the Pacific MHW are accompanied by a north–south oscillation of the jet stream position and opposite phase of SSTA patterns over the North Atlantic, indicating different associations between the North Pacific and the North Atlantic.

It is possible that the different wave train paths of the two variants give rise to the opposite phases of the Atlantic tripolar SST pattern or that the different Atlantic SST conditions induce different wave sources in the tropical Pacific to excite the different wave train paths. Previous research on the AMO impacts on the Pacific climate has suggested that the tripolar SSTA pattern of the AMO can influence the Pacific climate through both tropical and subtropical mechanisms. Under the tropical mechanism (Lyu and Yu 2017; Johnson et al. 2020; Meehl et al. 2021; Yao et al. 2021), the warm (cold) SSTA center in the tropical tripolar pattern can induce an anomalous descending (ascending) motion over the central tropical Pacific through a weakened (strengthened) Walker circulation (McGregor et al. 2014; Cai et al. 2019). The resulting anomalous cooling (heating) arises from weakened (strengthened) convection in the central tropical Pacific. The central tropical cooling in Pacific can excite a tropical Gill-type response and contribute to the warming of the Pacific Ocean in the

western-central equatorial region. The heating in the central (western-central) tropical Pacific can excite a Rossby wave train in midlatitude propagating to the North Pacific, resembling the basinwide wave train related to the GOA (COJ) variant of the MHW conditioning mode (see Figs. 7b,c). On the other hand, the subtropical mechanism (Sun et al. 2017; Ruprich-Robert et al. 2017) involves a direct impact from the subtropical warming/cooling center of the AMO. The center can directly induce an anomalous descending center over the northwestern Pacific. This leads to suppressed/enhanced convective activities, causing ocean surface warming and forming an SST–SLP–longwave radiative feedback that further induces temperature anomalies in the subtropical northwestern Pacific. This present study suggests that significant interbasin associations may be involved in the formation and long-lasting duration of North Pacific MHWs. The fact that MHW events occur more frequently during positive AMO phases than negative AMO phases further suggests a potential role of interbasin associations in the dynamics of the Pacific MHWs. Therefore, our findings suggest that interbasin associations between the North Pacific and North Atlantic play a crucial role in the occurrence of Pacific MHW events and in shaping their structures.

A few important issues were not addressed in this study and require future extensive studies. First, we need to understand why there exist the two preferred wave train paths in the North Pacific that, respectively, drive the GOA and COJ variants of the MHW conditioning mode. Second, it is not yet clear what feedback(s) may result from the Atlantic SSTAs inducing the MHW conditioning mode in the North Pacific, and whether the interactions play a role in prolonging the MHW durations. A better understanding of this possible role may enable us to predict the occurrence of Pacific MHW events and better prepare for their impacts. An obvious limitation of our study is that most of the results are based on reanalysis data with varying lengths, ranging from decades to about 150 years. Therefore, our conclusions still need to be supported by further elucidation to explain the connection mechanism between basin-scale MHWs in the North Pacific and North Atlantic Oceans.

Acknowledgments. We would also like to express our gratitude to Editor Stephen Yeager and three anonymous reviewers for their constructive comments, which have greatly contributed to the improvement of this paper. This study was supported by the NSF Climate and Large-Scale Dynamics Program under Grant AGS-2109539.

Support for the Twentieth Century Reanalysis Project dataset is provided by the U.S. Department of Energy, Office of Science Innovative and Novel Computational Impact on Theory and Experiment (DOE INCITE) program, and Office of Biological and Environmental Research (BER), and by the National Oceanic and Atmospheric Administration Climate Program Office.

Data availability statement. The Twentieth Century Reanalysis Project dataset is available at https://psl.noaa.gov/data/gridded/data.20thC_ReanV2.html. The NCEP Global Ocean Data Assimilation System (GODAS) is available at https://psl.noaa.gov/data/gridded/data.godas.html. The NCEP-NCAR Reanalysis 1 data are available at https://psl.noaa.gov/data/gridded/data.ncep.reanalysis.html. The HadISST data are available at https://www.metoffice.gov.uk/hadobs/hadisst/data/download.html.

REFERENCES

Amaya, D. J., N. E. Bond, A. J. Miller, and M. J. DeFlorio, 2016: The evolution and known atmospheric forcing mechanisms behind the 2013–2015 North Pacific warm anomalies. *U.S. CLIVAR Variations*, No. 14 (2), International CLIVAR Project Office, Southampton, United Kingdom, 1–6, https://usclivar.org/newsletters.

——, A. J. Miller, S.-P. Xie, and Y. Kosaka, 2020: Physical drivers of the summer 2019 North Pacific marine heatwave. *Nat. Commun.*, **11**, 1903, https://doi.org/10.1038/s41467-020-15820-w.

——, M. A. Alexander, A. Capotondi, C. Deser, K. B. Karnauskas, A. J. Miller, and N. J. Mantua, 2021: Are long-term changes in mixed layer depth influencing North Pacific marine heatwaves? *Bull. Amer. Meteor. Soc.*, **102** (Suppl.), S59–S66, https://doi.org/10.1175/BAMS-D-20-0144.1.

Barnston, A. G., and R. E. Livezey, 1987: Classification, seasonality and persistence of low-frequency atmospheric circulation patterns. *Mon. Wea. Rev.*, **115**, 1083–1126, https://doi.org/10.1175/1520-0493(1987)115<1083:CSAPOL>2.0.CO;2.

Behringer, D., and Y. Xue, 2004: Evaluation of the global ocean data assimilation system at NCEP: The Pacific Ocean. *Proc. Eighth Symp. on Integrated Observing and Assimilation Systems for Atmosphere, Oceans, and Land Surface*, Seattle, WA, Amer. Meteor. Soc., 11–15.

Bond, N. A., J. E. Overland, M. Spillane, and P. Stabeno, 2003: Recent shifts in the state of the North Pacific. *Geophys. Res. Lett.*, **30**, 2183, https://doi.org/10.1029/2003GL018597.

——, M. F. Cronin, H. Freeland, and N. Mantua, 2015: Causes and impacts of the 2014 warm anomaly in the NE Pacific. *Geophys. Res. Lett.*, **42**, 3414–3420, https://doi.org/10.1002/2015GL063306

Cai, W., and Coauthors, 2019: Pantropical climate interactions. *Science*, **363**, eaav4236, https://doi.org/10.1126/science.aav4236.

Chen, Z., J. Shi, Q. Liu, H. Chen, and C. Li, 2021: A persistent and intense marine heatwave in the northeast Pacific during 2019–2020. *Geophys. Res. Lett.*, **48**, e2021GL093239, https://doi.org/10.1029/2021GL093239.

Cheung, W. W. L., and T. L. Frölicher, 2020: Marine heatwaves exacerbate climate change impacts for fisheries in the northeast Pacific. *Sci. Rep.*, **10**, 6678, https://doi.org/10.1038/s41598-020-63650-z.

Compo, G. P., and Coauthors, 2011: The Twentieth Century Reanalysis Project. *Quart. J. Roy. Meteor. Soc.*, **137** (654), 1–28, https://doi.org/10.1002/qj.776.

Cronin, M. F., and Coauthors, 2013: Formation and erosion of the seasonal thermocline in the Kuroshio Extension Recirculation Gyre. *Deep-Sea Res. II*, **85**, 62–74, https://doi.org/10.1016/j.dsr2.2012.07.018.

Deser, C., and M. L. Blackmon, 1995: On the relationship between tropical and North Pacific sea surface temperature variations. *J. Climate*, **8**, 1677–1680, https://doi.org/10.1175/1520-0442(1995)008<1677:OTRBTA>2.0.CO;2.

Di Lorenzo, E., and N. Mantua, 2016: Multi-year persistence of the 2014/15 North Pacific marine heatwave. *Nat. Climate Change*, **6**, 1042–1047, https://doi.org/10.1038/nclimate3082.

——, and Coauthors, 2008: North Pacific Gyre Oscillation links ocean climate and ecosystem change. *Geophys. Res. Lett.*, **35**, L08607, https://doi.org/10.1029/2007GL032838.

Ding, R., J. Li, Y. Tseng, C. Sun, and Y. Guo, 2015: The Victoria mode in the North Pacific linking extratropical sea level pressure variations to ENSO. *J. Geophys. Res. Atmos.*, **120**, 27–45, https://doi.org/10.1002/2014JD022221.

Frölicher, T. L., and C. Laufkötter, 2018: Emerging risks from marine heat waves. *Nat. Commun.*, **9**, 650, https://doi.org/10.1038/s41467-018-03163-6.

Ge, Z.-A., L. Chen, T. Li, and M. Sun, 2023: Unraveling the formation mechanism of exceptionally strong marine heatwave in the northeast Pacific in 2020. *J. Climate*, **36**, 8091–8111, https://doi.org/10.1175/JCLI-D-22-0947.1.

Gentemann, C. L., M. R. Fewings, and M. García-Reyes, 2017: Satellite sea surface temperatures along the West Coast of the United States during the 2014–2016 northeast Pacific marine heat wave. *Geophys. Res. Lett.*, **44**, 312–319, https://doi.org/10.1002/2016GL071039.

Hall, R., R. Erdélyi, E. Hanna, J. M. Jones, and A. A. Scaife, 2015: Drivers of North Atlantic polar front jet stream variability. *Int. J. Climatol.*, **35**, 1697–1720, https://doi.org/10.1002/joc.4121.

Hassan, W. U., and M. A. Nayak, 2020: Global teleconnections in droughts caused by oceanic and atmospheric circulation patterns. *Environ. Res. Lett.*, **16**, 014007, https://doi.org/10.1088/1748-9326/abc9e2.

Hobday, A. J., and Coauthors, 2016: A hierarchical approach to defining marine heatwaves. *Prog. Oceanogr.*, **141**, 227–238, https://doi.org/10.1016/j.pocean.2015.12.014.

Hu, Z.-Z., A. Kumar, B. Jha, J. Zhu, and B. Huang, 2017: Persistence and predictions of the remarkable warm anomaly in the northeastern Pacific Ocean during 2014–16. *J. Climate*, **30**, 689–702, https://doi.org/10.1175/JCLI-D-16-0348.1.

Huang, B., Y. Xue, D. Zhang, A. Kumar, and M. J. McPhaden, 2010: The NCEP GODAS ocean analysis of the tropical Pacific mixed layer heat budget on seasonal to interannual time scales. *J. Climate*, **23**, 4901–4925, https://doi.org/10.1175/2010JCLI3373.1.

Hurrell, J. W., Y. Kushnir, G. Ottersen, and M. Visbeck, 2003: An overview of the North Atlantic oscillation. *The North Atlantic Oscillation: Climatic Significance and Environmental Impact*, *Geophys. Monogr.*, Vol. 134, Amer. Geophys. Union, 35 pp., https://doi.org/10.1029/134GM01.

Johnson, Z. F., Y. Chikamoto, S.-Y. S. Wang, M. J. McPhaden, and T. Mochizuki, 2020: Pacific decadal oscillation remotely forced by the equatorial Pacific and the Atlantic Oceans. *Climate Dyn.*, **55**, 789–811, https://doi.org/10.1007/s00382-020-05295-2.

Josey, S. A., J. J.-M. Hirschi, B. Sinha, A. Duchez, J. P. Grist, and R. Marsh, 2018: The recent Atlantic cold anomaly: Causes, consequences, and related phenomena. *Annu. Rev. Mar. Sci.*, **10**, 475–501, https://doi.org/10.1146/annurev-marine-121916-063102.

Kalnay, E., and Coauthors, 1996: The NCEP/NCAR 40-Year Reanalysis Project. *Bull. Amer. Meteor. Soc.*, **77**, 437–472, https://doi.org/10.1175/1520-0477(1996)077<0437:TNYRP>2.0.CO;2.

Kuroda, H., and T. Setou, 2021: Extensive marine heatwaves at the sea surface in the northwestern Pacific Ocean in summer 2021. *Remote Sens.*, **13**, 3989, https://doi.org/10.3390/rs13193989.

Liang, Y.-C., J.-Y. Yu, E. S. Saltzman, and F. Wang, 2017: Linking the tropical Northern Hemisphere pattern to the Pacific warm blob and Atlantic cold blob. *J. Climate*, **30**, 9041–9057, https://doi.org/10.1175/JCLI-D-17-0149.1.

Lyu, K., and J.-Y. Yu, 2017: Climate impacts of the Atlantic multidecadal oscillation simulated in the CMIP5 models: A reevaluation based on a revised index. *Geophys. Res. Lett.*, **44**, 3867–3876, https://doi.org/10.1002/2017GL072681.

Mantua, N. J., and S. R. Hare, 2002: The Pacific decadal oscillation. *J. Oceanogr.*, **58**, 35–44, https://doi.org/10.1023/A:1015820616384.

McGregor, S., A. Timmermann, M. F. Stuecker, M. H. England, M. Merrifield, F.-F. Jin, and Y. Chikamoto, 2014: Recent Walker circulation strengthening and Pacific cooling amplified by Atlantic warming. *Nat. Climate Change*, **4**, 888–892, https://doi.org/10.1038/nclimate2330.

Meehl, G. A., and Coauthors, 2021: Atlantic and Pacific tropics connected by mutually interactive decadal-timescale processes. *Nat. Geosci.*, **14**, 36–42, https://doi.org/10.1038/s41561-020-00669-x.

Minobe, S., and N. Mantua, 1999: Interdecadal modulation of interannual atmospheric and oceanic variability over the North Pacific. *Prog. Oceanogr.*, **43**, 163–192, https://doi.org/10.1016/S0079-6611(99)00008-7.

Nie, Y., H.-L. Ren, and Y. Zhang, 2019: The role of extratropical air–sea interaction in the autumn subseasonal variability of the North Atlantic Oscillation. *J. Climate*, **32**, 7697–7712, https://doi.org/10.1175/JCLI-D-19-0060.1.

Nishida, T., T. Kitakado, H. Matsuura, and S. P. Wang, 2011: Validation of the Global Ocean Data Assimilation System (GODAS) data in the NOAA National Centre for Environmental System (NCEP) by theory, comparative studies, applications and sea truth. Indian Ocean Tuna Commission Rep. IOTC-2011-WPB09-11, 18 pp., http://www.iotc.org/documents/validation-global-ocean-data-assimilation-system-godas-data-noaa-national-centre.

Peterson, W., M. Robert, and N. Bond, 2015: The warm blob continues to dominate the ecosystem of the northern California Current. *PICES Press*, North Pacific Marine Science Organization, Sidney, BC, Canada, 23, 44–46, https://www.pices.int/publications/pices_press/volume23/PPJuly2015.pdf.

Rayner, N. A., D. E. Parker, E. B. Horton, C. K. Folland, L. V. Alexander, D. P. Rowell, E. C. Kent, and A. Kaplan, 2003: Global analyses of sea surface temperature, sea ice, and night marine air temperature since the late nineteenth century. *J. Geophys. Res.*, **108**, 4407, https://doi.org/10.1029/2002JD002670.

Robinson, C. J., 2016: Evolution of the 2014–2015 sea surface temperature warming in the central west coast of Baja California, Mexico, recorded by remote sensing. *Geophys. Res. Lett.*, **43**, 7066–7071, https://doi.org/10.1002/2016GL069356.

Rodwell, M. J., and C. K. Folland, 2002: Atlantic air–sea interaction and seasonal predictability. *Quart. J. Roy. Meteor. Soc.*, **128**, 1413–1443, https://doi.org/10.1002/qj.200212858302.

Ruprich-Robert, Y., R. Msadek, F. Castruccio, S. Yeager, T. Delworth, and G. Danabasoglu, 2017: Assessing the climate impacts of the observed Atlantic multidecadal variability using the GFDL CM2.1 and NCAR CESM1 global coupled models. *J. Climate*, **30**, 2785–2810, https://doi.org/10.1175/JCLI-D-16-0127.1.

Scannell, H. A., G. C. Johnson, L. Thompson, J. M. Lyman, and S. C. Riser, 2020: Subsurface evolution and persistence of marine heatwaves in the northeast Pacific. *Geophys. Res. Lett.*, **47**, e2020GL090548, https://doi.org/10.1029/2020GL090548.

Schmeisser, L., N. A. Bond, S. A. Siedlecki, and T. P. Ackerman, 2019: The role of clouds and surface heat fluxes in the maintenance of the 2013–2016 northeast Pacific marine heatwave. *J. Geophys. Res. Atmos.*, **124**, 10 772–10 783, https://doi.org/10.1029/2019JD030780.

Shi, H., and Coauthors, 2022: Global decline in ocean memory over the 21st century. *Sci. Adv.*, **8**, eabm3468, https://doi.org/10.1126/sciadv.abm3468.

Shi, J., C. Tang, Q. Liu, Y. Zhang, H. Yang, and C. Li, 2022: Role of mixed layer depth in the location and development of the northeast Pacific warm blobs. *Geophys. Res. Lett.*, **49**, e2022GL098849, https://doi.org/10.1029/2022GL098849.

Shi, Y., B. Wang, and W. Huang, 2017: A 'self-adjustment' mechanism for mixed-layer heat budget in the equatorial Atlantic cold tongue. *Atmos. Sci. Lett.*, **18**, 82–87, https://doi.org/10.1002/asl.728.

Simmons, A. J., J. M. Wallace, and G. W. Branstator, 1983: Barotropic wave propagation and instability, and atmospheric teleconnection patterns. *J. Atmos. Sci.*, **40**, 1363–1392, https://doi.org/10.1175/1520-0469(1983)040<1363:BWPAIA>2.0.CO;2.

Sun, C., F. Kucharski, J. Li, F.-F. Jin, I.-S. Kang, and R. Ding, 2017: Western tropical Pacific multidecadal variability forced by the Atlantic multidecadal oscillation. *Nat. Commun.*, **8**, 15998, https://doi.org/10.1038/ncomms15998.

Swain, D. L., M. Tsiang, M. Haugen, D. Singh, A. Charland, B. Rajaratnam, and N. S. Diffenbaugh, 2014: The extraordinary California drought of 2013/2014: Character, context, and the role of climate change [in "Explaining Extreme Events of 2013 from a Climate Perspective"]. *Bull. Amer. Meteor. Soc.*, **95** (Suppl.), S3–S7, https://doi.org/10.1175/1520-0477-95.9.S1.1.

Takaya, K., and H. Nakamura, 2001: A formulation of a phase-independent wave-activity flux for stationary and migratory quasigeostrophic eddies on a zonally varying basic flow. *J. Atmos. Sci.*, **58**, 608–627, https://doi.org/10.1175/1520-0469(2001)058<0608:AFOAPI>2.0.CO;2.

Vijith, V., P. N. Vinayachandran, B. G. M. Webber, A. J. Matthews, J. V. George, V. K. Kannaujia, A. A. Lotliker, and P. Amol, 2020: Closing the sea surface mixed layer temperature budget from in situ observations alone: Operation Advection during BoBBLE. *Sci. Rep.*, **10**, 7062, https://doi.org/10.1038/s41598-020-63320-0.

von Biela, V. R., and Coauthors, 2022: Premature mortality observations among Alaska's Pacific salmon during record heat and drought in 2019. *Fisheries*, **47**, 157–168, https://doi.org/10.1002/fsh.10705.

Werb, B. E., and D. L. Rudnick, 2023: Remarkable changes in the dominant modes of North Pacific sea surface temperature. *Geophys. Res. Lett.*, **50**, e2022GL101078, https://doi.org/10.1029/2022GL101078.

Whitney, F. A., 2015: Anomalous winter winds decrease 2014 transition zone productivity in the NE Pacific. *Geophys. Res. Lett.*, **42**, 428–431, https://doi.org/10.1002/2014GL062634.

Yao, S.-L., W. Zhou, F.-F. Jin, and F. Zheng, 2021: North Atlantic as a trigger for Pacific-wide decadal climate change. *Geophys. Res. Lett.*, **48**, e2021GL094719, https://doi.org/10.1029/2021GL094719.